J Mater Sci (2017) 52:8556–8567

High sinterability nano-Y_2O_3 powders prepared via decomposition of hydroxyl-carbonate precursors for transparent ceramics

Le Zhang[1,4,5], Zheng Li[1,2], Fangzheng Zhen[1], Lixi Wang[2], Qitu Zhang[2], Rong Sun[3], Farida A. Selim[4,*], Chingping Wong[5], and Hao Chen[1,*]

[1] *Jiangsu Key Laboratory of Advanced Laser Materials and Devices, School of Physics and Electronic Engineering, Jiangsu Normal University, Xuzhou 221116, People's Republic of China*

[2] *College of Materials Science and Engineering, Nanjing Tech University, Nanjing 210009, People's Republic of China*

[3] *Guangdong Provincial Key Laboratory of Materials for High Density Electronic Packaging, Shenzhen Institutes of Advanced Technology, Chinese Academy of Sciences, Shenzhen 518055, People's Republic of China*

[4] *Department of Physics and Astronomy, Center for Photochemical Sciences, Bowling Green State University, Bowling Green, OH 43403, USA*

[5] *School of Materials Science and Engineering, Georgia Institute of Technology, Atlanta, GA 30332, USA*

Received: 27 February 2017
Accepted: 30 March 2017
Published online: 3 April 2017

ABSTRACT

High sinterability nano-Y_2O_3 powders for transparent ceramics were successfully synthesized via the decomposition of hydroxyl-carbonate precursors from spray coprecipitation. The chemical composition of the precursor was determined as $Y(CO_3)(OH)\cdot nH_2O$ (n = 1–1.5), and it was evolved into Y_2O_3 particles with clear facets after calcination with the assistance of sulfate. Two dispersion mechanisms, "absorption" and "intercalation," were proposed to work together to provide the dispersion effect. Microstructural and optical characterization of powders and as-fabricated transparent ceramics was employed to evaluate the sintering behavior of powders. The nanopowders calcined at 1250 °C had weakly agglomerated morphology with the mean particle size of ~140 nm and exhibited excellent sinterability. The in-line transmittance of Y_2O_3 ceramic of 1 mm thickness that was vacuum sintered at 1800 °C for 8 h without any sintering additives reached 78.7% at 1064 nm.

Introduction

Cubic Y_2O_3 has excellent physical and chemical properties, such as high corrosion resistivity, high melting point, and excellent optical transparency. However, it is quite difficult to fabricate large size Y_2O_3 single crystals due to the high melting point and the phase transition at ~2350 °C. Therefore, Y_2O_3 transparent ceramics have been developed and applied in various fields such as high-temperature

Address correspondence to E-mail: faselim@bgsu.edu; chenhao@jsnu.edu.cn

DOI 10.1007/s10853-017-1071-0

resistance windows, solid-state lasers, and semiconductors [1–3]. Compared with single crystals, the transparent ceramics have many advantages, such as the possibility of fabricating large size samples at low cost and achieving high concentration and homogeneous doping of rare earth ions [4, 5].

High-quality Y_2O_3 transparent ceramics can be obtained from full densification and pore-free microstructure [6, 7]. Generally, the densification of transparent ceramics significantly depends on two challenging issues. The first one is sintering process, and it is easily controlled by optimizing system temperature, pressure, atmosphere, and sintering additives [8–10]. However, the second one is the sinterability of raw powders and it is hard to control because it depends on many factors such as purity morphology, and particle size, especially the agglomeration of particles [11]. But this point is clear that the agglomeration of nanopowders never benefits to the densification of ceramics due to the uncontrollable and inconsistent grain boundary mobility [12, 13]. Therefore, the synthesis of high dispersibility nanopowders is crucial for the fabrication of high-quality Y_2O_3 transparent ceramics [14]. Although transparent ceramics with high optical transparency can be fabricated by adding sintering additives [15, 16], the aliovalent substitution of Y^{3+} by sintering additives such as LiF, HfO_2, ThO_2, and ZrO_2 would lead to the formation of cation/anion vacancies and defect clusters. These defects have a detrimental effect on laser performance [17, 18]. In fact, high optical transparency of transparent ceramics with a lower amount of sintering additives or without any is always pursued as the ideal medium for solid-state lasers.

Previous efforts have mainly focused on the effect of different synthesis methods on the powder properties, such as sol–gel method [19], hydrothermal synthesis [20], and coprecipitation method [21, 22]. Generally, the coprecipitation method often results in serious agglomeration and particle size with wide distribution. The drop-by-drop feed style produces big droplets, and the local concentrations of metal ions or precipitants are relatively high, leading to fast nucleation and growth. In addition, the precipitated precursor itself and its evolution into oxide powders during the calcination process also have significant impacts on the laser performance [23]. Because the calcination includes water removing, organic or intermediate phase decomposition, the phase crystallization and especially accompanying agglomeration [24, 25].

In this study, the novel spray coprecipitation method was used to synthesize Y_2O_3 powders using ammonium sulfate $(NH_4)_2SO_4$ as the dispersant in solution. This spray coprecipitation could separate the processes of the nucleation and growth. This separation is always negligible, and it is not possible to realize in the conventional coprecipitation method. Thus, the properties of the precursor would be greatly different from that by the conventional coprecipitation. Using this approach, the well-dispersed Y_2O_3 nanopowders with high sinterability were successfully synthesized through the decomposition of hydroxyl-carbonate precursors in this study. The composition of precursors and the action mechanism of $(NH_4)_2SO_4$ as a dispersant were determined. Furthermore, the influence of calcination temperature on the morphology, particle size, phase composition, and agglomeration of Y_2O_3 powders was studied in details and the microstructure and optical properties of as-prepared Y_2O_3 ceramics vacuum sintered at 1800 °C were also systematically investigated to evaluate the sintering behaviors of powders in the case of without any sintering additives.

Materials and experimental details

Synthesis of nanocrystalline Y_2O_3 powders

High-purity yttrium oxide (Y_2O_3, 99.99%, Alfa Aesar, Ward Hill, MA) was selected as the starting material. The mixed solution of 1.0 mol/L ammonium hydrogen carbonate (NH_4HCO_3, AHC) and 1.5 mol/L ammonia water ($NH_3{\cdot}H_2O$, AW) was used as the combined precipitant. Nitric acid (HNO_3) was used to dissolve Y_2O_3 powders, and ammonium sulfate $(NH_4)_2SO_4$ was used as the dispersant. All used chemicals were analytical grade from Aladdin chemicals, Shanghai, China. $Y(NO_3)_3$ solution was prepared by dissolving yttria powders into nitric acid and diluted with distilled water until the solution concentration reached 0.15 mol/L; then, $(NH_4)_2SO_4$ ($[SO_4^{2-}]/[Y^{3+}] = 30$ mol%) was added into the $Y(NO_3)_3$ solution.

The spray coprecipitation device was composed of an air compressor to provide the driving force for the spraying process, four air filters to eliminate

impurities from the compressed air, an atomizer to atomize the precipitant, and a peristaltic pump to control the rate of the precipitant. The combined precipitants were sprayed into the $Y(NO_3)_3$ solution at the rate of 2 ml/min and stirred at room temperature until the final pH reached 8.0. After spraying, the precipitates were aged for 12 h to obtain Y_2O_3 precursors. The obtained precursors were filtrated and washed firstly with deionized water for three times and then with ethanol for another three times. Finally, the washed precursors were dried at 60 °C for 24 h in an oven and then calcined at 1100, 1150, 1200, 1250, and 1300 °C for 4 h in air to obtain nanocrystalline Y_2O_3 powders.

Fabrication of Y_2O_3 ceramics

The calcined Y_2O_3 powders were sieved through a 150-mesh screen and then dry-pressed into Φ16-mm disks in a stainless steel mold under 25 MPa, followed by cold isostatic pressing under 200 MPa for 5 min. After removing the residue organics at 800 °C for 4 h in a muffle furnace, the green bodies were sintered at 1450–1600 °C for 4 h in air to check the sinterability of nanocrystalline powders and then vacuum sintered at 1800 °C for 8 h in a vacuum furnace under 10^{-3} Pa to complete densification. Finally, the sintered Y_2O_3 ceramics were annealed at 1100 °C in air for 10 h to fill oxygen vacancies, and then, two sides were ground and polished to 1 mm.

Characterizations

The phases of Y_2O_3 powders calcined under different temperatures were identified by X-ray diffraction (XRD, D2, Bruker, Germany) measurements. Specific surface areas S(BET) of the powders were measured with an accelerated surface area and porosimetry system (Model Micromeritics ASAP2010, Norcross, USA) using N_2 gas. The element compositions of the powders were performed by X-ray fluorescence spectrometer (XRF, Waltham, USA) and elemental analyzer (Vario ELcube CHONS). The morphologies of powders and microstructures of ceramics were studied by a scanning electron microscope (SEM, JSM-6510, JEOL, Japan) and transmission electron microscope (TEM, G2, FEI Tecnai, USA). The relative densities of Y_2O_3 ceramics were measured and calculated by the Archimedes method. The in-line transmittance of transparent ceramics was measured using a UV–VIS–NIR spectrophotometer (Lambda 950, PerkinElmer, Waltham, MA, America) in the wavelength range of 200–1200 nm.

Results and discussion

Figure 1 shows the SEM images of Y_2O_3 powders under the different calcination temperatures. It can be seen that the calcination temperature has a significant effect on the morphology, particle size, and agglomeration of the powders. The mean particle size of the powders increased from ~50 to ~170 nm with increasing the calcination temperature from 1100 to 1300 °C. It was clear that, after calcination at different temperatures, all powders showed good crystallinity (as shown later), but the serious agglomeration still existed when the calcination temperature was below 1200 °C. This agglomeration was attributed to the small particle size and the high surface energy of the powders calcined at low temperature. With the increase in calcination temperature, the shape of particles became more clear with obvious facets and round edge. However, when the calcination temperature reached 1300 °C, the mass diffusion became fast and this led to the formation of sintering neck, which indicated an excessive sintering and the reduction in surface energy of particles. This would result in the loss of sintering activity of the powders. The powders with weakly agglomerated morphology and good dispersibility were synthesized when the calcination temperature was 1250 °C and the mean particle sizes were ~140 nm.

Generally, the agglomeration state of powders was evaluated according to the following equation [23]: $n = (D_{BET}/D_{XRD})^3$, where n is the agglomeration parameter, and the smaller of the parameter n, the weaker the agglomeration state of powders. Figure 2 shows the specific surface area (S_{BET}), the corresponding particle size D_{BET}, the grain size (D_{XRD}) calculated by Sherrer's formula, and the change of n value with the calcination temperature. The grain size of Y_2O_3 powders was calculated using the X-ray line broadening method performed on the three strongest diffraction peaks of (2 2 2), (4 0 0), and (4 4 0) according to the Sherrer's formula: $D_{XRD} = 0.89\lambda/(\beta \cos \theta)$. Here, λ is the wavelength of CuKα (0.15406 nm), and β is the full-width at half-maximum (FWHM) of a diffraction peak at Bragg angle θ. The specific surface area was converted to particle

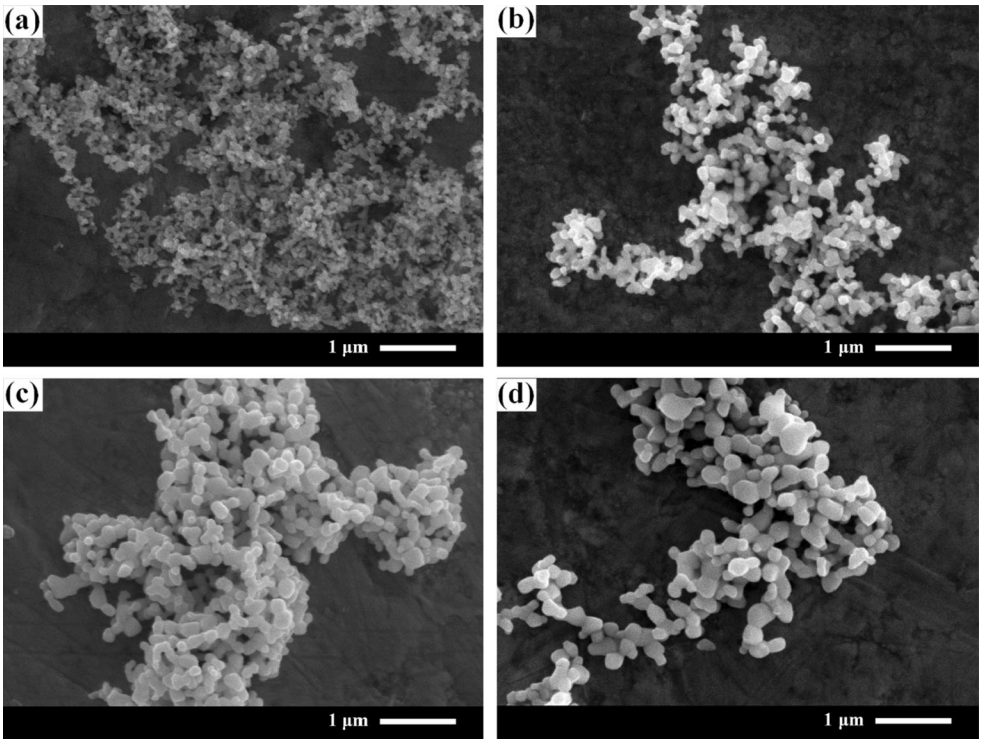

Figure 1 SEM images of Y_2O_3 powders under different calcination temperatures: **a** 1100 °C, **b** 1200 °C, **c** 1250 °C, and **d** 1300 °C.

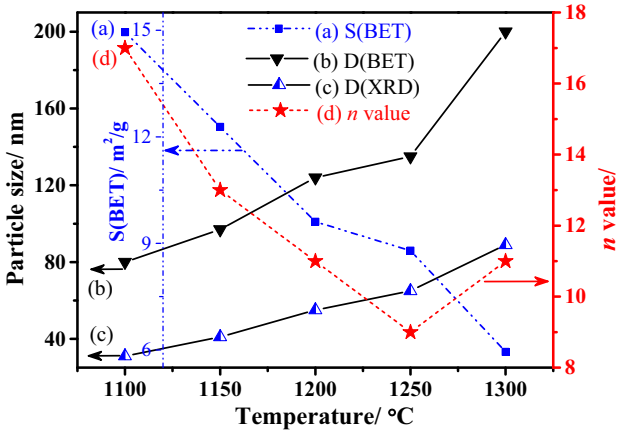

Figure 2 BET, particle sizes (from BET and XRD), and n value of the powders under different calcination temperatures.

size using this equation: $D_{BET} = 6/(\rho \cdot SBET)$. Here, it is assumed that the particle shape is a closed sphere with the smooth surface and uniform size and ρ is the theoretical density of Y_2O_3 (5.03 g/cm^3). As shown in Fig. 2a, the specific surface area of Y_2O_3 powders decreased from ~15.0 to 6.0 m^2/g with increasing the calcination temperature, and both D_{BET} and D_{XRD} were increased due to the agglomeration of the particles and grain growth (Fig. 2b, c). However, the relatively faster increase of D_{BET} happened especially above 1250 °C (Fig. 2b). It is noted that the particle size obtained from the specific area was about two times larger than that measured by XRD method, indicating the existence of agglomeration of powders. The calculated n value was smallest when the calcination temperature was 1250 °C (Fig. 2b) and was largest when the temperature was 1100 °C. It is well known [19, 26] that the powders calcined below 1000 °C often have large specific surface area and a large number of adsorbates and they cannot be easily compacted into the uniform green body. On the other hand, the calcination temperature above 1300 °C easily causes severe agglomeration and loses some sinterability of the powder.

Therefore, Y_2O_3 powders calcined at 1250 °C for 4 h are the most suitable for preparing transparent ceramics with high optical quality. Figure 3a shows TEM image of Y_2O_3 powders calcined at 1250 °C, all powders were very uniform, and most particles were composed of coadjacent grains with a mean diameter of 80–100 nm, which aggregated to be a chain in one-dimensional space. This slight agglomeration could be easily destroyed when the powders are in the forming stages of green body by dry pressing or cold isostatic pressing of 200 MPa, during which the plastic flow and deformation would occur to fill the

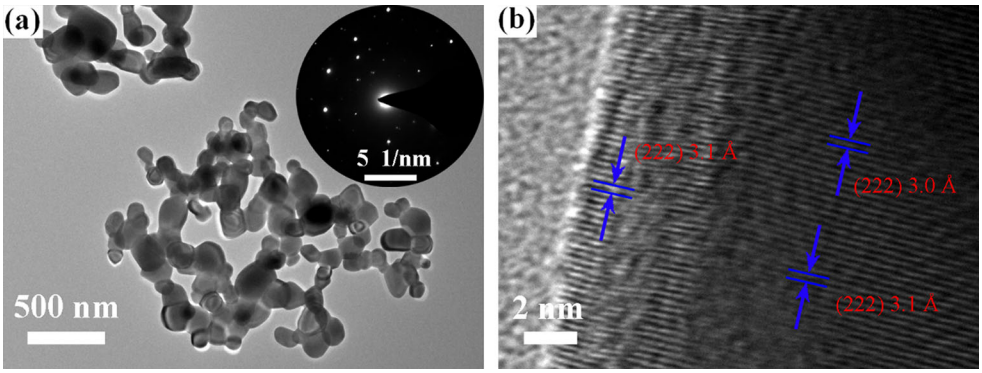

Figure 3 **a** TEM image of Y_2O_3 powders calcined at 1250 °C (*inset* selected area electron diffraction image), **b** high-resolution TEM image showing the lattice planes (*d*-spacing: (222)-3.1 Å).

interspace between particles to get the high initial density of the green body. Therefore, this slight agglomeration would have little effect on the sintering activity. The grains also displayed pseudo-spherical shape with clear facets and rough edges. These nanocrystalline powders exhibited the better dispersibility and favored to the preparation of high-quality Y_2O_3 ceramics with fine microstructure [27]. In addition, the selected area electron diffraction pattern (Fig. 3a inset)) revealed that the powders were cubic Y_2O_3 with lattice parameter 10.604 Å, and this result was in agreement with XRD measurements as shown below. The high-resolution TEM image (Fig. 3b) showed the clear lattice fringes separated by 3.1 Å, which corresponded to the (222) plane of Y_2O_3. It is worth mentioning that the morphology and the particle size of the as-prepared Y_2O_3 powders are greatly different under different calcination temperatures, and this results in the significant difference in the microstructure and optical transparency of fabricated ceramics. The result of subsequent sintering experiments proved that the powder calcined at 1250 °C has the highest sinterability.

Furthermore, the phase compositions of the precursor and Y_2O_3 powders under different calcination temperatures are identified by XRD in Fig. 4. After the calcination of Y_2O_3 powders, the characteristic diffraction peaks corresponded to cubic yttria phase (JCPDS: 41-1105) were sharp, indicating the good crystallinity. With the increase in calcination temperature, the intensity of the characteristic diffraction peaks was increased and the full-width at half-maximum (FWHM) became narrow, indicating the enhanced crystallinity and larger grain size. The grain size was increased from 36.0 to 89.0 nm as the

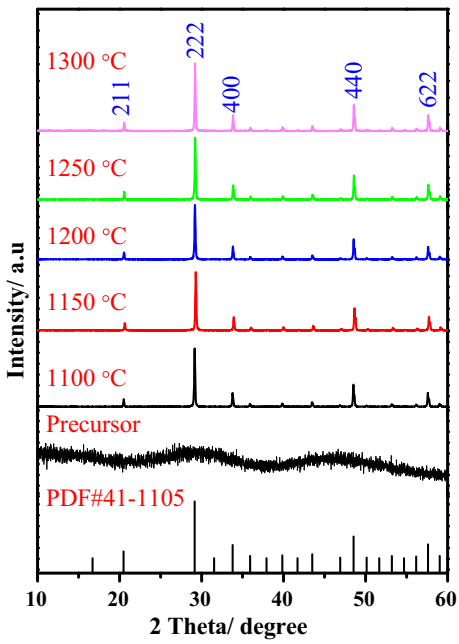

Figure 4 XRD patterns of the precursor and Y_2O_3 powders under different calcination temperatures.

calcination temperature increased from 1100 to 1300 °C in Fig. 2. It can be noted that the as-synthesized precursor in this study is amorphous, which is in agreement with previous reports [14, 28]. However, some other previous studies showed that the precursors can be crystalline even their crystallinity degrees were lower [12, 29]. In Liu's study [29], the precursor was well indexed as $Y_2(CO_3)_3{\cdot}2.79\ H_2O$ (JCPDS: 54-0624) when only AHC (1.0 mol/L) was used as a precipitant. But in Yavetskiy study [12], the precursor composition was $Y_2(OH)_5(NO_3)_{1-x-y}(CO_2)_x\ (SO_4)_y{\cdot}nH_2O$ ($n = 1$–2), in which only AW (2.0 mol/L) was used as the precipitant. In this study,

AHC and AW were together used as the combined precipitant and resulted in the amorphous phase. This is an interesting phenomenon, and its mechanism needs to be further investigated. However, it is very clear that the phase composition of precursors has a strong relationship with the precipitant composition and its concentration, the dispersant effect, and the pH value at the end of precipitation process. The evolution process from precursor to oxide powders during the calcination process has the different chemical reactions and morphology changes and at last affects the sintering activity. In addition, it is crucial to determine the precise chemical composition of precursors.

The FTIR spectra of yttria powders under different calcination temperatures are shown in Fig. 5. All calcined powders displayed the similar FTIR shape. The single broad peak at 3700–2800 cm^{-1} was attributed to the stretching vibrations of OH^{-1}, and the double peaks at ~1520 and ~1425 cm^{-1} resulted from $v3$ C–O asymmetric and symmetric stretching vibration of CO_3^{2-}. Several peaks between 850 and 600 cm^{-1} in the fingerprint region were attributed to the out of plane bending vibrations of CO_3^{2-}. OH^- and CO_3^{2-} groups are associated with the H_2O and CO_2 absorbed from the air [30]. The peaks at ~1115 and 620 cm^{-1} were attributed to the vibration of SO_4^{2-}, and the relative intensity of these two peaks decreased with increasing the temperature. This indicates the decrease of SO_4^{2-} content. The peaks near 560 cm^{-1} were ascribed to the vibrations of Y–O bonds. The 1400 cm^{-1} band associated with vibrations of NH_4^+ was not observed in all spectra indicating an effective washing process and the complete absence of NH_4^+ ions. In addition, all peaks corresponded to water and carbonates in Fig. 5 still remained even after the high-temperature calcination. It is impossible that these molecules existed at such high temperatures. Therefore, we expect that a fast hydration reaction occurred after the calcination in all cases due to the large specific surface (~10 m^2/g, Fig. 2). The water molecules from air moisture strongly interacted with the surface of Y_2O_3 and gradually incorporated into the surface layer and formed a "bulk hydroxide layer" at the room temperature. Then, the alkaline surface layer of yttria strongly reacts with CO_2 adsorbed from the air and formed the carbonate (or hydroxyl-carbonate).

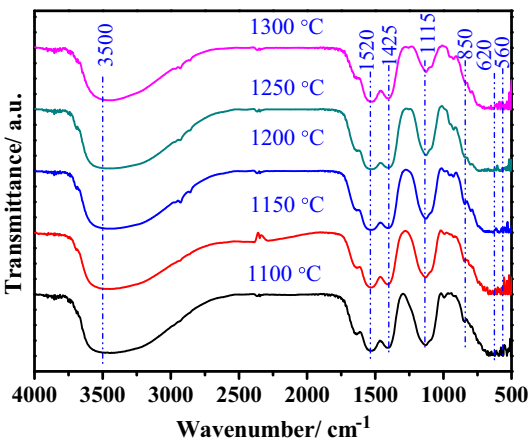

Figure 5 FTIR spectra of Y_2O_3 powders under different calcination temperatures.

In our experiment, the weights of the precursor before and after calcination at 1250 °C were 36.5 and 20.3 g, respectively. The mass loss was 44.4%, which was caused by the removal of water and CO_2. The element contents of N, C, H, S in precursor and powders from the elemental analyzer are shown in Table 1. According to the weight of powders and the element contents, the mole of Y, H, C element was 0.18, 0.77, and 0.20 mol, respectively, and the ratio of n(H)/n(C) was 3.8. Accordingly, the chemical composition of the precursor was calculated and found to be $Y(CO_3)(OH)\cdot nH_2O$ ($n = 1$–1.5). The content of SO_4^{2-} decreased with the increase in calcination temperature as indicated in Table 2. Moreover, in this study, the S element composition in the precursor was 1.881 wt%, and the weight of precursor was

Table 1 Element amounts in precursor and powders calcined at 1250 °C from elemental analyzer

Elements	N	C	H	S
Precursor (wt%)	0	6.48	2.096	1.881
Powders (wt%)	0	0.32	0.907	0.479

Table 2 Element compositions of powders calcined at different temperatures from XRF

Temperature/°C	Y/wt%	O/wt%	S/wt%
1100	75.25	23.06	1.690
1150	76.79	22.38	0.822
1200	78.57	20.67	0.757
1250	78.67	20.82	0.512
1300	78.81	21.12	0.075

36.5 g. Therefore, the mole of SO_4^{2-} was 0.022 mol. The mole of the SO_4^{2-} (0.022 mol) in precursor was less than that (0.068 mol) in the raw material because the SO_4^{2-} was scoured off during the washing process. The negatively charged SO_4^{2-} had the strong electrostatic attraction with the positive precursor surfaces [31]. The saturated coverage of SO_4^{2-} ions on the Y_2O_3 particle surfaces was effective to inhibit the agglomeration and the growth of nuclei [32]. Therefore, this explains why the mole of SO_4^{2-} (0.068 mol) in the raw solution is higher than its value (0.022 mol) in the precursor, and the left SO_4^{2-} group was sufficiently absorbed on the surface of the precursor.

In addition, there was no N element in the composition of precursor, indicating that all the NO_3^- ions were washed away. There was still S element even in the powders calcined at temperatures as high as 1250 °C. This is consistent with the results in Fig. 5. The high decomposition temperature of sulfate ions can inhibit the aggregation and the fast growth of the crystallite grains, resulting in the good dispersion and narrow particles distribution [28, 33].

In fact, $(NH_4)_2SO_4$ has been widely used in the coprecipitation method to obtain high dispersibility nanocrystalline Y_2O_3 powders. However, the sulfate role and its evolution in coprecipitation process have always been a controversial issue and there are many questions that have never been answered. First, how does the sulfate affect the nucleation and growth processes? Second, whether could it be partly or totally removed by the washing treatment? Third, what does the dispersant happen during the calcination and how does its residual content affect the optical properties? Huang et al. [28] employed AHC as the precipitant and added the sulfate into the solution before coprecipitation, and kept the pH of the reaction system at 8.3. They found there was hardly any sulfate remaining in the precursors and concluded that the sulfate played an important role in the control of particle shape of the precursors during the formation process rather than during the high-temperature calcination. Generally, SO_4^{2-} groups formed the ion pairs with the high valence metal ions by the intensive electrostatic attraction, and when AHC was added, CO_3^{2-} groups competed with SO_4^{2-} groups for metal ions, and then, the resultant carbonate nucleated into the small amorphous particles. Its tetrahedral configuration and steric hindrance of SO_4^{2-} retarded the further growth in some directions of the amorphous powders and led to the needle shape of precursors because these directions had higher positive charge density. This means SO_4^{2-} groups only had a big impact on the small amorphous particles and less influence on the growing precursors. For the washing step, the precursors were electrical neutrality, and the main interaction between SO_4^{2-} and precursors was van der Waals force and it was much weaker than the electrostatic attraction. Thus, sulfate was almost removed through washing for several times.

However, Yavetskiy [12] reported the totally different results. They found that the intercalation of sulfate ions into the interlayer of $Y_2(OH)_5NO_3{\cdot}nH_2O$ structure formed the $Y_2(OH)_5(NO_3)_{1-x-y}(CO_2)_x(SO_4)_y{\cdot}nH_2O$ through the physical adsorption effect and van der Waals force. SO_4^{2-} groups aligned gradually along the crystallographic axes, thereby exhibiting the specific crystallographic contours, and this isotropic surface of precursor had no special crystallographic orientation to induce unusually rapid or slow particle growth. They also found that the upper limit temperature of quasi-spherical particles (1100 °C) was equal to the temperature of desulfurization. Because sulfate slows down diffusion process that prevents nanopowders from coarsening, agglomeration and sintering. They concluded that even relatively low sulfur concentration at 1100 °C (0.17 wt%) retarded diffusion mass transport and resulted in weakly agglomerated primary particles of ~50 nm.

These two kinds of action mechanism of sulfate discussed above are named "absorption mechanism" and "intercalation mechanism," respectively. They are summarized in Table 3. It is clearly concluded that the action mechanism of sulfate in the precipitation is dependent on the precipitant type and its different adding points (before or after the precipitation). They affected the morphology and size of precursor and calcined powders. Other works have supported the same conclusions [14, 29, 32, 33]. In the present study, AHC and AW are combined as the mixed precipitants and the precipitate composition is determined as $Y(CO_3)(OH){\cdot}nH_2O$ ($n = 1$–1.5). These two dispersion mechanisms work together to play the dispersion role and lead to the weakly agglomerated nanopowders with high sinterability. Furthermore, we developed the selection principles of the dispersant in the coprecipitation method. The first principle is that the surfactant should be thermally stable and

Table 3 Comparison of two different action mechanisms of sulfate in coprecipitation

	Absorption mechanism	Intercalation mechanism
Precipitant	NH_4HCO_3	$NH_3{\cdot}H_2O$
Precipitate	$Y_2(CO_3)_3{\cdot}2H_2O$	$Y_2(OH)_5(NO_3)_{1-x-y}(CO_2)_x(SO_4)_y{\cdot}nH_2O$
Adding timing of sulfate	Before coprecipitation	After
Precursor shape	From big compact into needle-like	To plate-like
Calcined shape	Agglomerated to dispersion, 50 nm	To individual crystals, 50 nm
Role in precipitation	Shape control of precursors during formation process rather than during calcination process	Just into structure, no other roles
Action mechanism	Attracted by some directions with higher positive charge density and then retarded further growth	Low sulfate at 1100 °C retarded diffusion mass transport
Saturation state	Adsorption onto nucleated particles	Saturation of interlayer region
Sulfate amount/	10 mol%	5 mol%
If remaining after washing	No any, after action, weaker van der Waals force	Yes, almost left in structure
If remaining after calcination	No	0.17 wt% 1100, near zero 1200 °C

can ultimately decompose into gas without introducing any impurity. The second is that the surfactant should have strong absorption effect with the precursor, high valence, and bigger group volume to play the role of dispersion. Obviously, more dispersants are needed to further improve the dispersibility.

From the above results, the calcination process had a significant effect on the particle morphology and size and the agglomeration state of the powders. In order to further study the effect of calcination on the sintering behaviors of the powders, we fabricated ceramics from the powders under different calcination temperatures.

Figure 6a shows the thermal mechanical curves of Y_2O_3 green compact from powders calcined at 1250 °C. The obvious shrinkage also began at about 1250 °C, and the biggest linear shrinkage rate occurred at ~1495 °C. Therefore, the starting sintering temperature of ceramics used to check the powders sinterability should be selected at around this temperature. Figure 6b shows the relative densities of ceramics air sintered at low temperatures to check the sintering activity of powders under different calcination temperatures. Obviously, the relative densities of ceramics from powders calcined at the same temperature increased with the increase in sintering temperatures from 1450 to 1600 °C. However, the relative densities of Y_2O_3 ceramics increased with the

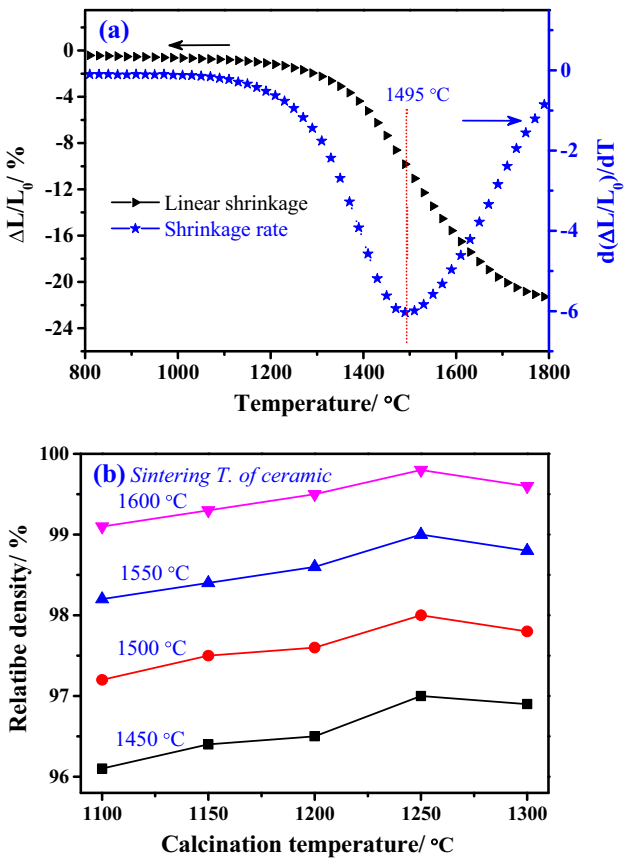

Figure 6 **a** Thermal mechanical analyzer curves of Y_2O_3 *green* compact from powders calcined at 1250 °C, **b** relative densities of Y_2O_3 ceramics from powders under different calcination temperatures.

increase in calcination temperatures and reached a maximum at about 1250 °C and then decreased at each sintering temperature. These results are in agreement with the agglomeration state of the powders (as shown in Figs. 1 and 2). The sintering activity of the nano powders is particularly sensitive to the agglomeration of the powders since the sintering driving force and the shrinkage inside agglomerates are different from those of between agglomerates. The Y_2O_3 ceramics from powders calcined at 1250 °C had the highest relative density at each sintering temperature because the agglomeration state was weak and no sintering necks appeared. The relative density of Y_2O_3 ceramics without any sintering additives from powders calcined at 1250 °C reached 99.6% only under the sintering temperature of 1600 °C, indicating the high sinterability of powders synthesized by a spray coprecipitation method.

The SEM images of the thermally etched surfaces of Y_2O_3 ceramics under different sintering temperature (from powders calcined at 1250 °C) are shown in Fig. 7. The average grain size of the ceramics sintered at 1450 °C in air was 0.55 μm, and the distribution of grain size was narrow, but the pores were large and connected together (Fig. 7a). When the sintering temperature reached 1500 °C, the average grain size of ceramics had a slight increase to 0.59 μm, but the number of intergranular pores dramatically decreased (Fig. 7b), and the pores were isolated. The number of pores was further reduced when the sintering temperature was 1550 °C and the average grain size increased to 0.70 μm (Fig. 7c). The pores in the ceramics sintered at 1600 °C were hard to observe (Fig. 7d), and the grain size increased rapidly to 0.95 μm. Figure 8 shows the sintering trajectory for Y_2O_3 ceramics between 1450 and 1600 °C for 4 h. The densification process was accompanied by the grain growth when the sintering temperature was below 1550 °C. However, the grain growth dominated the densification process when the sintering temperature was above 1550 °C. Figures 7d and 8 show the abnormal growth for the ceramics sintered at 1600 °C.

Figure 9 shows the in-line transmittance of the ceramics fabricated from powders under different calcination temperatures and then vacuum sintered at 1800 °C for 8 h and annealed at 1100 °C for 10 h in air. The inset in Fig. 9 is the corresponding

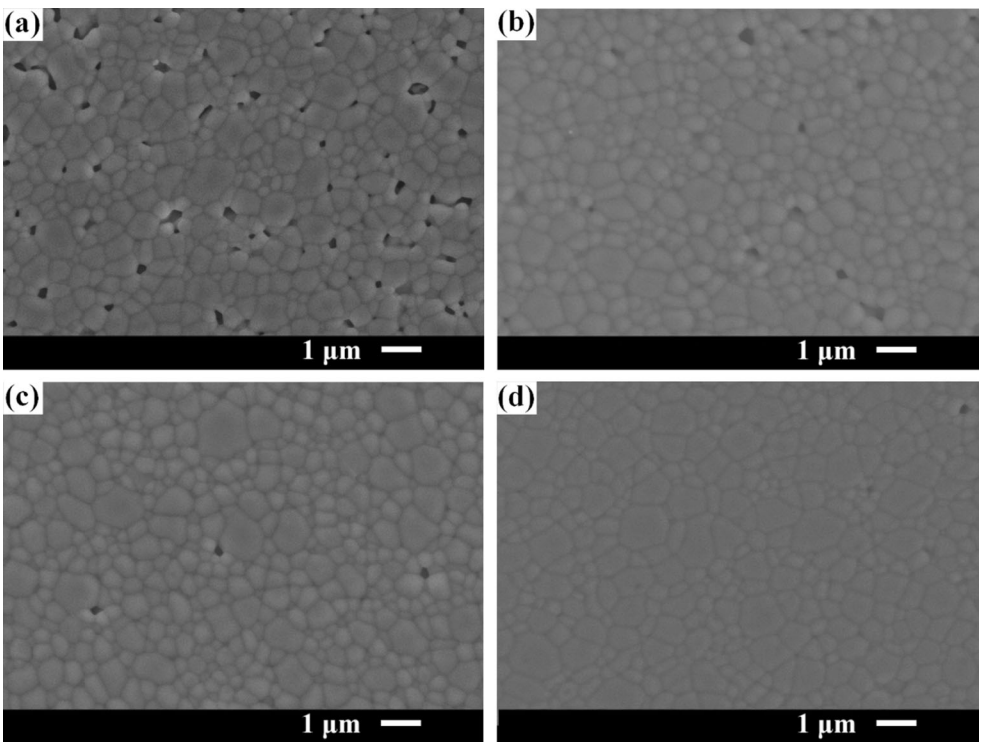

Figure 7 SEM images of the thermally etched surfaces of air-sintered Y_2O_3 ceramics at **a** 1450 °C, **b** 1500 °C, **c** 1550 °C, and **d** 1600 °C for 4 h.

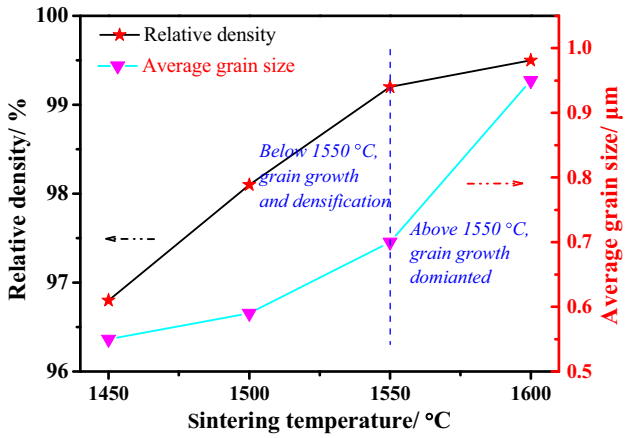

Figure 8 Sintering trajectory for Y_2O_3 ceramics sintered between 1450 and 1600 °C for 4 h.

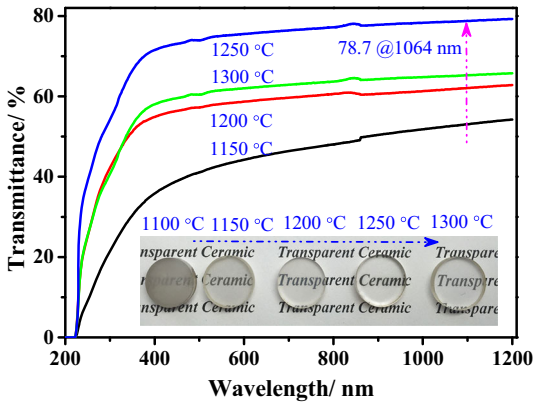

Figure 9 In-line transmittance of Y_2O_3 ceramics (1 mm thickness) vacuum sintered at 1800 °C for 8 h from powders calcined under different temperatures.

photographs of the ceramics. The transmittance of the ceramics fabricated from powders calcined at 1100 °C was very low due to the serious agglomeration of the powders. When the calcination temperatures increased from 1100 to 1150 °C and 1200 °C, the agglomeration state of the powders decreased, and the transmittance was enhanced from 53.0 to 62.7% (at 1064 nm). The transmittance of ceramics fabricated from powders calcined at 1250 °C reached 78.7%, owing to the high sinterability of the powders. The excessive sintering occurred when it further increased to 1300 °C. In this case, the transmittance was reduced to 65.2%. Furthermore, the transmittance decreased more rapidly at the wavelength below 400 nm. This means the presence of small pores as the scattering centers. The transmittance has a close relationship with the calcination temperature because the latter has a significant effect on the morphology and agglomeration of powders. The appropriate calcination of the precursor is crucial to prepare high sintering activity powders for transparent ceramics.

Conclusions

Nanocrystalline Y_2O_3 powders with high sinterability were synthesized by the decomposition of hydroxyl-carbonate precursors from a spray coprecipitation route. The chemical composition of the precursor was determined as $Y(CO_3)(OH)\cdot nH_2O$ ($n = 1$–1.5), and it was evolved into Y_2O_3 particles with clear facets after calcination. The calcination temperature had a significant effect on the agglomeration and particle size of powders. The powders had the weak agglomeration and good dispersibility when the calcination temperature was 1250 °C and its mean particle size was ~140 nm. Sulfate still existed in powders after calcination at 1250 °C, and two kinds of dispersion mechanism of "absorption" and "intercalation" were proposed to work together to play the dispersion role. Y_2O_3 powders calcined at 1250 °C had the high sinterability, and the relative density of ceramics air sintered at 1600 °C reached 99.6%. The in-line transmittance of ceramics sintered at 1800 °C for 8 h in vacuum without any sintering additives was 78.7% at 1064 nm.

Acknowledgements

The authors acknowledge the generous financial support from the National Natural Science Foundation of China (51402133, 51202111, 11274144), Priority Academic Program Development of Jiangsu Higher Education Institutions (PAPD), Guangdong Provincial Key Laboratory (2014B030301014), Research and Innovation Program for College Graduates of Jiangsu Province (KYZZ16_0231), and Special Project for Technology Innovation of Xuzhou City (KC16GZ014, KC16HQ236, KC16HQ237).

References

[1] Ikesue A, Yan LA (2008) Ceramic laser materials. Nat Photonics 5:721–727

[2] Jacobsohn LG, Serivalsatit K, Quarles CA, Ballato J (2015) Investigation of Er-doped Sc_2O_3 transparent ceramics by positron annihilation spectroscopy. J Mater Sci 50:3183–3188. doi:10.1007/s10853-015-8881-8

[3] Chen C, Li XL, Feng Y, Lin H, Yi XZ, Tang YR, Zhang S, Zhou SM (2015) Optimization of CeO_2 as sintering aid for $Tb_3Al_5O_{12}$ Faraday magneto-optical transparent ceramics. J Mater Sci 50:2517–2521. doi:10.1007/s10853-014-8810-2

[4] Chen X, Lu T, Wei N, Lu Z, Chen L, Zhang Q, Cheng G, Qi J (2015) Fabrication and photoluminescence properties of Cr: YAG and Yb, Cr: YAG transparent ceramic. Opt Mater 49:330–336

[5] Zhang L, Ben Y, Wu J, Yang H, Wong C, Zhang Q, Chen H (2017) Alumina assisted grain refinement and physical performance enhancement of yttria transparent ceramics by two-step sintering. Mater Sci Eng A 684:466–469

[6] Zhang L, Yang H, Qiao X, Zhou T, Wang Z, Zhang J, Tang D, Shen D, Zhang Q (2015) Systematic optimization of spray drying for YAG transparent ceramics. J Eur Ceram Soc 35:2391–2401

[7] Xiong Y, Fu ZY, Wang YC, Quan F (2006) Fabrication of transparent AIN ceramics. J Mater Sci 41:2537–2539. doi:10.1007/s10853-006-5314-8

[8] Zhang XR, Fan GF, Wang XH, Lei W, Fei L, Lu WZ (2016) Effects of sintering parameters and Nd doping on the microwave dielectric properties of Y_2O_3 ceramics. Ceram Int 42:7962–7967

[9] Wang ZY, Zhang L, Yang H, Zhang J, Wang LX, Zhang QT (2016) High optical quality Y_2O_3 transparent ceramics with fine grain size fabricated by low temperature air pre-sintering and post-HIP treatment. Ceram Int 42:4238–4245

[10] Frage N, Cohen S, Meir S, Kalabukhov S, Dariel MP (2007) Spark plasma sintering (SPS) of transparent magnesium-aluminate spinel. J Mater Sci 42:3273–3275. doi:10.1007/s10853-007-1672-0

[11] Zhang XR, Lu WZ, Fan GF, Wang XH (2016) Fabrication of well-dispersed Y_2O_3 nano-powders by poly(acrylic acid) low-temperature combustion. Adv Powder Technol 27:295–298

[12] Yavetskiy RP, Kosyanov DY, Baumer VN, Doroshenko AG, Fedorov AI, Matveevskaya NA, Tolmachev AV, Vovk OM (2014) Low-agglomerated yttria nanopowders via decomposition of sulfate-doped precursor with transient morphology. J Rare Earth 32:320–325

[13] Zhang L, Ben Y, Chen H, Tang D, Fu X, Sun R, Song B, Wong C (2017) Low temperature-sintering and microstructure of highly transparent yttria ceramics. J Alloys Compd 695:2580–2586

[14] Huang Z, Sun X, Xiu Z, Chen S, Tsai CT (2004) Precipitation synthesis and sintering of yttria nanopowders. Mater Lett 58:2137–2142

[15] Wang J, Zhang J, Ning KJ, Luo DW, Yang H, Yin DL, Tang DY, Kong LB (2016) Densification of yttria transparent ceramics: the utilization of activated sintering. J Am Ceram Soc 99:1671–1675

[16] Shan ZF, Chen DQ, Yu YL, Huang P, Lin H, Wang YS (2010) Luminescence in rare earth-doped transparent glass ceramics containing GdF_3 nanocrystals for lighting applications. J Mater Sci 45:2775–2779. doi:10.1007/s10853-010-4266-1

[17] Wang ZY, Zhang L, Yang H, Zhang J, Wang LX, Zhang QT (2016) Effect of gamma-Al_2O_3 additives on the microstructure of Y_2O_3 ceramics. J Mater Sci Mater Electron 27:3384–3389

[18] Guo Y, Wang D, Wu X, Wang Q, He Y (2016) Novel fabrication, microstructure and upconversion photoluminescence properties of Tm^{3+}, Yb^{3+} co-doped Y_2O_3 translucent ceramics. J Alloys Compd 688:816–819

[19] Xu SQ, Li J, Li CY, Pan YB, Guo JK (2015) Infrared-transparent Y_2O_3–MgO nanocomposites fabricated by the glucose sol-gel combustion and hot-pressing technique. J Am Ceram Soc 98:2796–2802

[20] Tanner PA, Fu L (2009) Morphology of Y_2O_3: Eu^{3+} prepared by hydrothermal synthesis. Chem Phys Lett 470:75–79

[21] Kabir M, Ghahari M, Afarani MS (2014) Co-precipitation synthesis of nano Y2 O3: Eu3+ with different morphologies and its photoluminescence properties. Ceram Int 40:10877–10885

[22] Kumar D, Sharma M, Pandey OP (2014) Effect of co-doping metal ions (Li^+, Na^+ and K^+) on the structural and photoluminescent properties of nano-sized Y_2O_3: Eu^{3+} synthesized by co-precipitation method. Opt Mater 36:1131–1138

[23] Liu Y, Qin X, Xin H, Song C (2013) Synthesis of nanostructured Nd: Y_2O_3 powders by carbonate-precipitation process for Nd: YAG ceramics. J Eur Ceram Soc 33:2625–2631

[24] Ragulya AV, Vasyl'Kiv OO, Skorokhod VV (1997) Synthesis and sintering of nanocrystalline barium titanate powder under nonisothermal conditions. I. Control of dispersity of barium titanate during its synthesis from barium titanyl oxalate. Powder Metall Met Ceram 36:170–175

[25] Tokariev O, Steinbrech RW, Schnetter L, Malzbender J (2012) Micro- and macro-mechanical testing of transparent $MgAl_2O_4$ spinel. J Mater Sci 47:4821–4826. doi:10.1007/s10853-012-6333-2

[26] Hajizadeh OM, Razavi RS, Barekat M, Naderi M, Malekzadeh S, Rezazadeh M (2016) Synthesis and characterization of Y_2O_3 nanoparticles by sol–gel process for transparent ceramics applications. J Solgel Sci Technol 78:682–691

[27] Li W, Kou HM, Chen M, Shi Y, Feng XQ, Pan YB, Guo JK (2014) Fabrication and characterization of grain-oriented cerium fluoride ceramics from a slip-casting process in a magnetic field. J Mater Sci 49:5030–5034. doi:10.1007/s10853-014-8207-2

[28] Huang Z, Guo W, Fei BJ, Li JT, Cao YG (2013) Influence of sulphate on synthesis of Nd: Y_2O_3 powders via coprecipitation route and fabrication of transparent ceramics. Mater Res Innov 17:73–79

[29] Liu B, Li J, Yavetskiy R, Ivanov M, Zeng Y, Xie T, Kou H, Zhuo S, Pan Y, Guo J (2015) Fabrication of YAG transparent ceramics using carbonate precipitated yttria powder. J Eur Ceram Soc 35:2379–2390

[30] Caro P, Sawyer J, Evning L (1972) The infrared spectra of rare earth carbonates. Spectrochim Acta A 28:1167–1173

[31] Li J, Li JP, Chen Q, Wu WJ, Xiao DQ, Zhu JG (2012) Effect of ammonium sulfate on the monodispersed $Y_3Al_5O_{12}$ nanopowders synthesized by co-precipitant method. Powder Technol 218:46–50

[32] He J, Li X, Liu S, Zhu Q, Li JG, Sun X (2015) Effects of pre-treatment of starting powder with sulfuric acid on the fabrication of yttria transparent ceramics. J Eur Ceram Soc 35:2369–2377

[33] Li SS, Liu BL, Li J, Zhu XW, Liu WB, Pan YB, Guo JK (2016) Synthesis of yttria nano-powders by the precipitation method: the influence of ammonium hydrogen carbonate to metal ions molar ratio and ammonium sulfate addition. J Alloys Compd 678:258–266